Nanoscale Horizons

ROYAL SOCIETY OF CHEMISTRY

COMMUNICATION

View Article Online
View Journal | View Issue

Cite this: *Nanoscale Horiz.*, 2025, **10**, 824

Received 25th October 2024,
Accepted 5th February 2025

DOI: 10.1039/d4nh00551a

rsc.li/nanoscale-horizons

Regulation of closed pores in hard carbon for enhanced electrochemical sodium storage†

Ziying Zhang,[a] Yingxinjie Wang,[b] Kejian Tang,[a] Zerui Chen,[b] Xiaohui Li,[b] Nan Zhang,[b] Zhenjun Wu*[a] and Xiuqiang Xie*[b]

The development of hard carbon materials with high plateau capacity as anode materials for sodium-ion batteries (SIBs) is crucial to improving the energy density of SIBs, while the closed pores are closely related to the low-voltage (<0.1 V) plateau capacity of hard carbon anodes. Herein, through a simple ZnO template method and acid treatment, a wealth of closed pores were created in the hard carbon material derived from camellia shells. Experimental results reveal the mechanism of sodium ions adsorption at the defect sites and the formation of sodium clusters in the closed pores, which corresponds to the slope region and the plateau region, respectively. Notably, being beneficial to the considerable closed pore content and suitable microstructure, the optimized sample exhibits a high reversible capacity of 340 mA h g^{-1}, which is mainly contributed by the low-voltage plateau process (51%). This work provides a new strategy for precisely regulating the microstructure of biomass-derived hard carbon for sodium-ion storage.

New concepts

Biomass hard carbons are being explored as anode materials for sodium-ion batteries due to the wide availability and excellent battery features. Among them, the design of hard carbons with abundant closed pores suitable for accommodating sodium clusters is an effective strategy to improve the plateau capacity at low voltage to improve the energy density of the actual full cell. In our work, the closed pore content and microstructure parameters (layer spacing, L_a, L_c, A_D/A_G) of biomass-derived hard carbon were precisely regulated to improve the electrochemical Na^+ storage performance, especially at low voltage. In order to further expand its commercialization potential, we assembled it with commercial $Na_3V_2(PO_4)_3$ (NVP) cathode material for full battery assembly, and finally demonstrated excellent cycling performance at high current density. These results further demonstrate the application potential of carbon materials with well-developed closed pores and provides insights into the microscopic structural regulation of closed pores in biomass-derived hard carbon materials.

Introduction

Lithium-ion batteries (LIBs) have been widely used in various fields because of their high energy density and long cycle life.[1–3] But the limited and unevenly distributed lithium resources limit their further application.[4–6] As alternatives to LIBs, the advantages of low cost and abundant resources endow sodium-ion batteries (SIBs) with great competitiveness.[7–10] However, graphite anodes, which are widely used in LIBs, are not suitable for SIBs due to the inherent kinetics and thermodynamic limitations.[11,12] In contrast, hard carbon materials can provide satisfactory sodium-ion storage capacity due to their abundant graphite microcrystals, defects and pores.[13–15] However, the complex structure of hard carbons makes it challenging to achieve precise structural regulation and improve the sodium storage capacity.[16–19]

During the working process of SIBs, the charge–discharge curve of hard carbon is mainly divided into two regions, the high-voltage slope region (>0.1 V) and the low-voltage plateau region (<0.1 V),[20,21] in which the performance in the low-voltage plateau region is essential to improve the energy density of the actual full cell.[22] Previous studies have shown that plateau capacity is closely related to closed pores filling of sodium ions.[23] The closed pores can not only improve the plateau capacity of hard carbons as effective active sites accommodating a large number of sodium ions, but also sieve out solvated sodium ions to limit the decomposition of electrolytes.[24,25] Therefore, it is an effective strategy to improve plateau capacity by designing hard carbon with abundant closed pores suitable for accommodating sodium clusters.[26–28] Increasing carbonization temperature is most commonly used to construct closed pores.[29] At higher temperatures, the highly active carbon radicals can be repaired and the conjugated carbon structures will be reorganized. Consequently, a large number of open pores will be transformed into closed pores.[30–32] However, the

[a] College of Chemistry and Chemical Engineering, Hunan University, Changsha 410082, P. R. China. E-mail: wooawt@hnu.edu.cn
[b] College of Materials Science and Engineering, Hunan University, Changsha 410082, P. R. China. E-mail: xiuqiang_xie@hnu.edu.cn

† Electronic supplementary information (ESI) available. See DOI: https://doi.org/10.1039/d4nh00551a

number of closed pores constructed by increasing the carbonization temperature is limited. Meanwhile, as the temperature increases, the sharp decrease in interlayer distance will limit the diffusion of sodium ions into closed pores, which is not conducive to the improvement of plateau capacity. Therefore, developing a simple and effective strategy to construct suitable porous structures remains a key factor in achieving high-capacity SIBs.

In this work, using camellia shells as raw material, hard carbon materials with high closed pores content and suitable microstructure were prepared by using the template method and acid treatment, which improved sodium-ion storage. The reversible capacity of the optimized hard carbon anode reached 340 mA h g^{-1} at 50 mA g^{-1}, in which the plateau capacity was 174 mA h g^{-1}, accounting for 51% of the total capacity. In addition, various characterization tests revealed that the high-voltage slope capacity and low-voltage plateau capacity were derived from the adsorption of sodium ions at the defect sites and the formation of sodium clusters in the closed pores, respectively.

This work highlights the application potential of carbon materials with well-developed closed pores and provides insights into the microscopic structural regulation of closed pores at the molecular level in biomass-derived hard carbon materials.

Experimental section

Materials preparation

The original camellia shells (CS) from Pingjiang County, Hunan Province were ball-milled into powder. The 1.2 g obtained powder and 0.1 g zinc acetate were dispersed in 15 mL deionized water, stirred at room temperature for 6 h, thoroughly mixed, centrifuged and freeze-dried. The dried sample was annealed at 600 °C for 2 h at a heating rate of 5 °C min^{-1} under an argon atmosphere. The intermediate product obtained is named ZCS6. Next, ZCS6 was placed in 1 mol L^{-1} hydrochloric acid solution at room temperature and stirred for 1 h, then washed with deionized water until pH = 7, dry at 60 °C, named ZHCS6. Finally, ZHCS6-13 was obtained by carbonizing ZHCS6 at 600 °C for 2 h at a heating rate of 5 °C min^{-1} in an argon atmosphere. ZCS6 is directly carbonized to obtain ZCS6-13, and HCS6-13 is prepared from powder that is not mixed with zinc acetate without any other steps being changed. The sample that was not mixed with zinc acetate and was not acid-treated and only carbonized by two steps was named CS6-13.

Material characterization

The morphologies and elemental mapping analysis of the hard materials were studied by field emission scanning electron microscopy (SEM, JEOLJSM-7800F, Japan) and transmission electron microscopy (TEM, FEI Titan G2 60–300) with energy dispersive X-ray spectroscopy (EDS). The X-ray diffraction (XRD, Rigaku Smart Lab, USA with Cu Kα radiation) analysis and Raman (WITec, alpha300 R with a 532 nm laser source) spectra were conducted to explore the crystal structures and degrees of graphitization for the hard materials. The chemical properties of the surface were investigated by X-ray photoelectron spectroscopy (XPS, Thermo Scientific K-Alpha). The sample porosity was analyzed by the N_2 absorption–desorption test (Micromeritics ASAP 2460) at 298 K, and the Brunauer–Emmett–Teller (BET) method was used to calculate the specific surface area. Closed pores were characterized by small-angle X-ray scattering (SAXS, Xenocs Xeuss 2.0). AccuPyc II 1340 instrument using helium as an analytical gas to measure the true density.

Electrochemical measurements

The CR-2023 button battery was assembled in an argon atmosphere glove box (H_2O < 0.01 ppm, O_2 < 0.01 ppm) for electrochemical measurements. The active material, acetylene black and polyvinylidene fluoride (PVDF) were mixed at 8 : 1 : 1 mass ratio and dispersed in an appropriate amount of *N*-methyl-2-pyrrolidone (NMP) to make a slurry. The slurry was then coated on the copper foil and dried under vacuum at 60 °C. Finally, the resulting electrode is cut into a 12 mm circular electrode. The half-cell uses sodium foil as the counter electrode, and glass fiber (Whatman, GF/F) and 1 M $NaClO_4$ in ethylene carbonate/diethyl carbonate (EC/DEC, 1 : 1 by volume) with 5 vol% addition of fluoroethylene carbonate (FEC) are selected as the separator and electrolyte, respectively. The galvanostatic charge/discharge profiles and galvanostatic intermittent titration technique (GITT) were carried out by the Land CT2001A system (Wuhan, China) in a voltage window of 0.01–2.8 V at 25 °C. The cyclic voltammetry (CV) measurements and electrochemical impedance spectroscopy (EIS) spectra were tested on an electrochemical workstation (CHI660E Chenhua, Shanghai) at scan rates of 0.1, 0.2, 0.4, 0.6, 0.8 and 1.0 mV s^{-1}. The sodium-ion full cells were assembled using a ZHCS6-13 anode and a commercial $Na_3V_2(PO_4)_3$ (NVP) cathode at an N/P ratio of 1–1.05 (the electrolyte and separator are the same as the half-cell). The voltage ranges of charge and discharge are 1.5–4 V for full cells.

Result and discussion

The synthesis process of ZHCS6-13 is illustrated in Fig. 1.

Typically, zinc acetate was mixed with the camellia shells after ball milling, and in the process of pre-carbonization at 600 °C, ZnO particles were formed in the precursor carbon as the nanopore templates. In the subsequent acid treatment stage, excess ZnO particles and ash in the precursor were removed, creating open pores at these locations. Finally, after high temperature carbonization at 1300 °C, the open pores gradually formed closed pores, and the ZnO embedded in the precursor carbon matrix catalyzed graphitization,[33] thereby promoting the development of graphite domains and facilitating the formation of closed pores. At the same time, ZnO is volatilized and removed at high temperature by carbothermal reaction ($ZnO + C \rightarrow Zn\uparrow + CO\uparrow$) to avoid excessive impurities in hard carbon affecting the electrochemical performance.[34–36] Moreover, for comparison, ZCS6-13 is not treated with

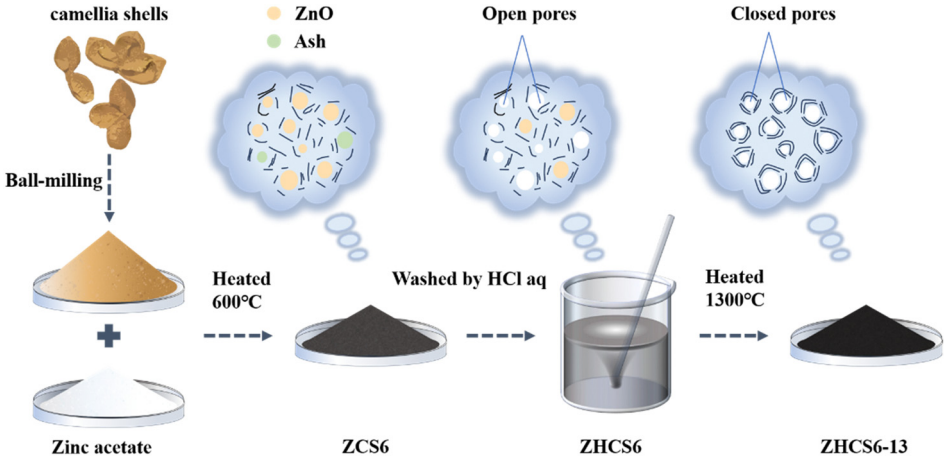

Fig. 1 Illustration of the synthesis procedures.

hydrochloric acid, and HCS6-13 is prepared from powder that is not mixed with zinc acetate with other steps unchanged. The sample prepared by the two-step carbonization but without zinc acetate and acid treatment was denoted as CS6-13.

The microstructure of the prepared samples was analyzed by scanning electron microscopy (SEM) and transmission electron microscopy (TEM). As shown in Fig. 2a–d, the four samples all show irregular morphology with similar particle sizes. TEM images show that the prepared samples are composed of turbostratic graphitic domains (blue dotted box) and nanopores of varied dimensions, including open pores and closed pores (yellow dotted circle), which can be regarded as the gap between the randomly oriented turbostratic graphite domains (Fig. 2e–h). In general, pores are open when their cavities and holes are connected with the outside of the porous solid, while pores in solids that don't communicate with the external surface and cannot be penetrated by fluids are defined as closed pores.[37,38] These closed pores facilitate the storage of sodium in the plateau region to form quasi-metallic sodium clusters.[39,40] These results are also evidence of the successful preparation of the hard carbon derived from camellia shells. In addition, Fig. S1 (ESI†) shows the carbon layer spacing measured by TEM, in which the average carbon layer spacing of ZHCS6-13, ZCS6-13, HCS6-13, and CS6-13 are 0.41, 0.39, 0.40, and 0.37 nm, respectively. It can be

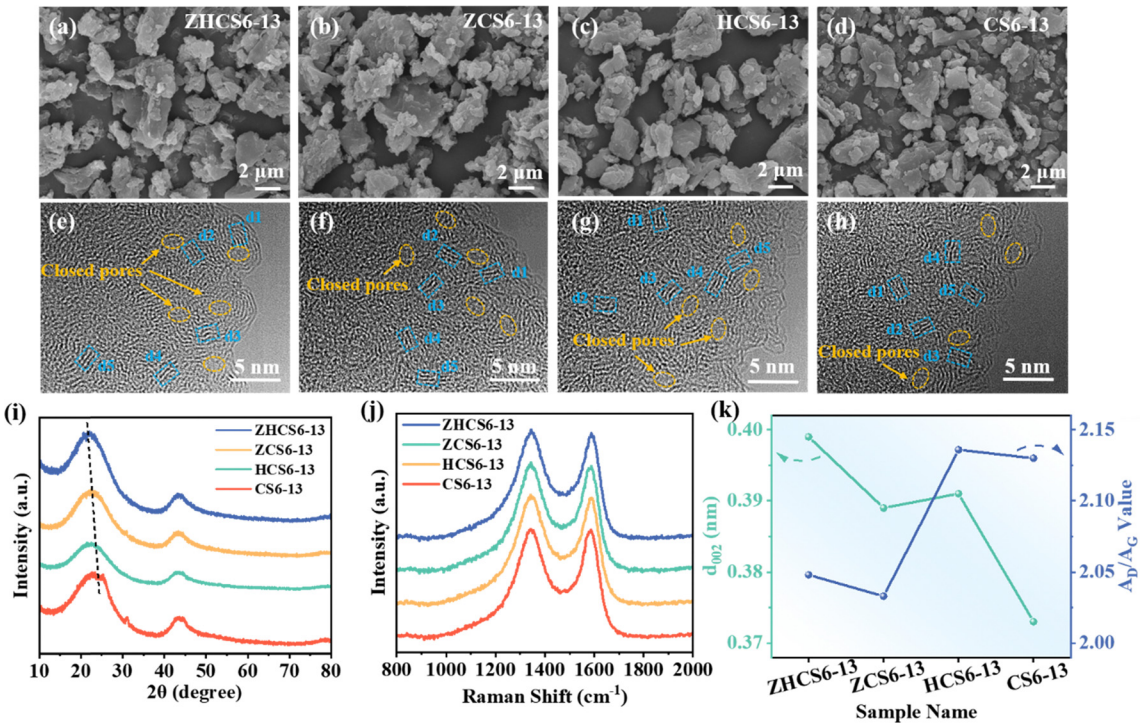

Fig. 2 SEM images of (a) ZHCS6-13, (b) ZCS6-13, (c) HCS6-13, (d) CS6-13. TEM images of (e) ZHCS6-13, (f) ZCS6-13, (g) HCS6-13, (h) CS6-13. (i) XRD patterns, (j) Raman spectra, and (k) fitted values of d_{002} and A_D/A_G of different samples.

seen that the carbon layer spacing increases both after the ZnO template method or acid treatment, which is conducive to the rapid transport of ions.

The XRD and Raman tests were carried out to further distinguish the microstructure of samples. As displayed in Fig. 2i, the XRD patterns of all samples show two broad diffraction peaks at ≈ 23° and ≈ 44°, which are associated with the (002) and (100) crystalline plane of the typical graphite nanodomains in the hard carbon, respectively.[41–43] Notably, the (002) peaks of the other three samples all shift to a lower degree compared with CS6-13, indicating an increase in interlayer distance,[44] which is consistent with the results measured through TEM (Fig. 2k and Fig. S1, ESI†). A peak at around 32° is observed in the XRD patterns of the samples without acid treatment (ZCS6-13 and CS6-13), but it disappears in the acid-treated sample (ZHCS6-13 and HCS6-13), which is related to the inorganic compositions of the raw material.[45] In addition, as shown in Fig. S2 (ESI†), the diffraction peaks of ZnO in ZHCS6 disappeared, indicating that most of the ZnO nanoparticles were removed after hydrochloric acid treatment. Meanwhile, the SEM image and the corresponding EDS mapping results further demonstrate the removal of ZnO on the surface of ZHCS6 (Fig. S3, ESI†). The residual ZnO is completely removed at a higher temperature carbonization of 1300 °C (Fig. 2i and Fig. S4, ESI†). Subsequently, to further analyze the microstructure changes of the samples, the Scherrer equations were used to calculate the average graphite domain length (L_a) and the graphite crystallite thickness (L_c).[46] As displayed in Table S1 (ESI†), compared with that of CS6-13 (L_a ≈ 4.20 nm, L_c ≈ 0.98 nm), the samples treated with zinc acetate (ZHCS6-13, ZCS6-13) have the largest L_a (4.25 nm, 4.35 nm), L_c (0.99 nm, 1.00 nm), which indicates that ZnO can effectively promote the development of graphite domains in hard carbons. In the samples only treated with acid (HCS6-13), L_a (3.95 nm) and L_c (0.96 nm) values were smaller than that of CS6-13, indicating that acid treatment can hinder the development of graphite domains to a certain extent. Modulation of the defect structure of hard carbon can improve the storage capacity of hard carbon and optimize the solid electrolyte interface (SEI) film.[47] Therefore, we further studied the surface defects of carbon materials using Raman spectroscopy. The Raman spectra of the samples are exhibited in Fig. 2j, where characteristic broad D and G peaks located at ~1345 and ~1590 cm^{-1} are assigned to disordered defects in the carbon layer and graphitic sp^2 carbon, respectively.[48,49] The Raman spectra were further fitted by the Gaussian function (Fig. S5, ESI†),[50] and the calculated area ratios of D-band and G-band (A_D/A_G) are shown in Fig. 2k, which is used to evaluate the disorder of carbon materials. ZHCS6-13 and ZCS6-13 exhibit smaller A_D/A_G values (2.05, 2.03) than CS6-13, (2.13) and HCS6-13 exhibits a larger A_D/A_G value (2.14) compared to CS6-13 (2.13), which is consistent with the XRD results, indicating that the ZnO particles in the samples can catalyze local graphitization, while the acid treatment alone increases the disorder of the samples. However, too high degree of graphitization or disorder is not conducive to sodium ions storage.[35,51] Therefore, the synthesized hard carbon only has the most suitable graphite domains and disorder when the biomass is treated simultaneously by acid treatment and ZnO template method. This is beneficial for the formation of larger interlayer spacing and abundant closed pores during the subsequent high temperature carbonization process, which provides the possibility to improve the sodium storage capacity.

To observe the specific surface area and pore structure of the open pores (connected to the external environment), N_2

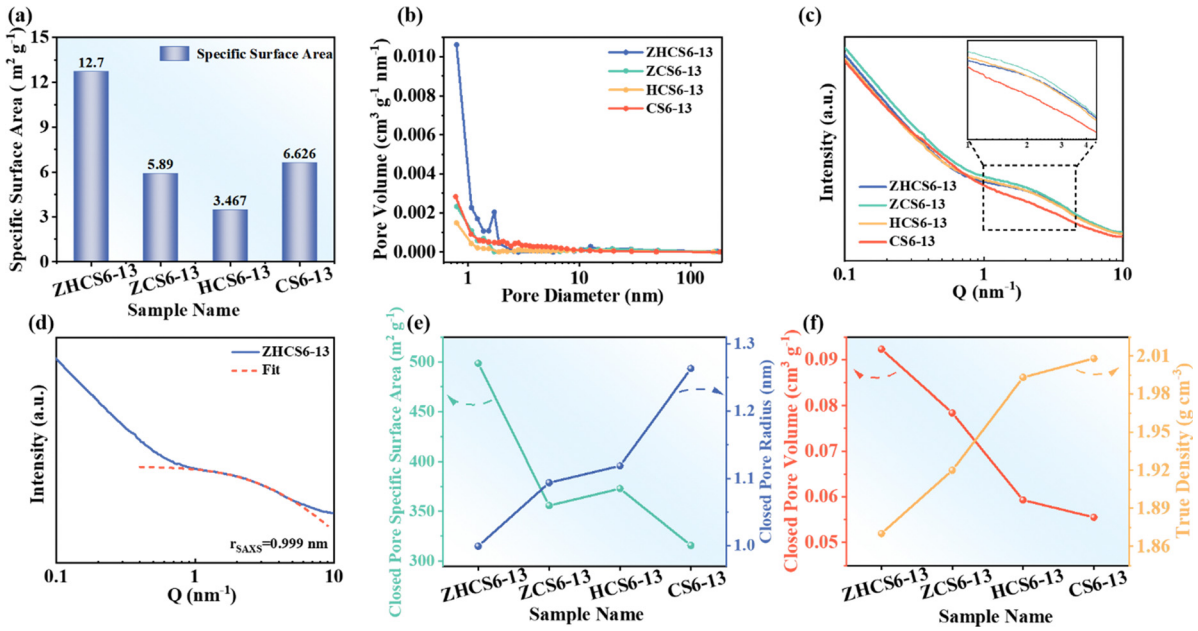

Fig. 3 (a) Specific surface area and (b) pore size distribution of samples. (c) SAXS spectra and (d) fitted SAXSs patterns of ZHCS6-13. (e) Specific surface area and the radius of closed pores calculated based on SAXS patterns. (f) True density and closed pore volume of samples.

adsorption–desorption tests were performed. As shown in Fig. 3a, b, Fig. S6 and Table S1 (ESI†), ZHCS6-13 has the largest specific surface area and the most abundant micropores, which are conducive to promoting the adsorption of sodium ions, thus promoting the penetration of electrolytes. The closed pore structure was investigated by small angle X-ray scattering (SAXS) and true density tests. As displayed in Fig. 3c, the four samples exhibit discernible shoulder peaks at about 0.1 $Å^{-1}$ derived from nanopore (including open pores and closed pores) scattering.[36,40] As shown in Fig. 3d, e, Fig. S7 and Table S1 (ESI†), the fitting and calculated results reveal that ZHCS6-13 has the smallest closed pore radius (r_{SAXS}). Closed pores with smaller radius are more conducive to sodium ions storage, mainly because the average sodium binding energy of small clusters is stronger and the interaction with the pore wall is enhanced, which is consistent with the ionic properties of sodium.[40,47] The total specific surface area (S_{SAXS}) from open pores and closed pores can be determined from the SAXS parameters using the semi-empirical Teubner–Strey model,[50,52] and by subtracting the specific surface area (S_{BET}) measured by N_2 adsorption–desorption, the closed pore specific surface area ($S_{closed\ pores}$) is obtained. As depicted in Fig. 3e, the closed pore surface area of ZHCS6-13, ZCS6-13, HCS6-13, and CS6-13 are 499, 356, 373, 315 $m^2\ g^{-1}$, respectively. Of all the samples, ZHCS6-13 has the largest $S_{closed\ pores}$, while CS6-13 has the smallest $S_{closed\ pores}$. It is speculated that under high temperature carbonization, ZnO catalyzes large graphite domains to shrink the pores and form closed pores, and acid treatment can also help to transform some open pores into closed pores. The synergistic effects make ZHCS6-13 have the largest specific surface area of closed pores, which is essential to achieve excellent electrochemical performance.

The true density test is a powerful complementary tool to SAXS, and the closed pore volume ($V_{closed\ pores}$) can be calculated by comparing the true density of hard carbon (ρ_{true}) with that of ideal graphite, which is considered to have no closed pores and provides the highest true density (2.26 g cm^{-3}).[25,26] As shown in Fig. 3f, the trend change of the closed pore volume is consistent with the SAXS results. These results show that the ZHCS6-13 has abundant closed pores suitable for sodium ions storage by the ZnO template method and acid treatment, which is conducive to improving the sodium storage capacity and further improving the electrochemical performance.

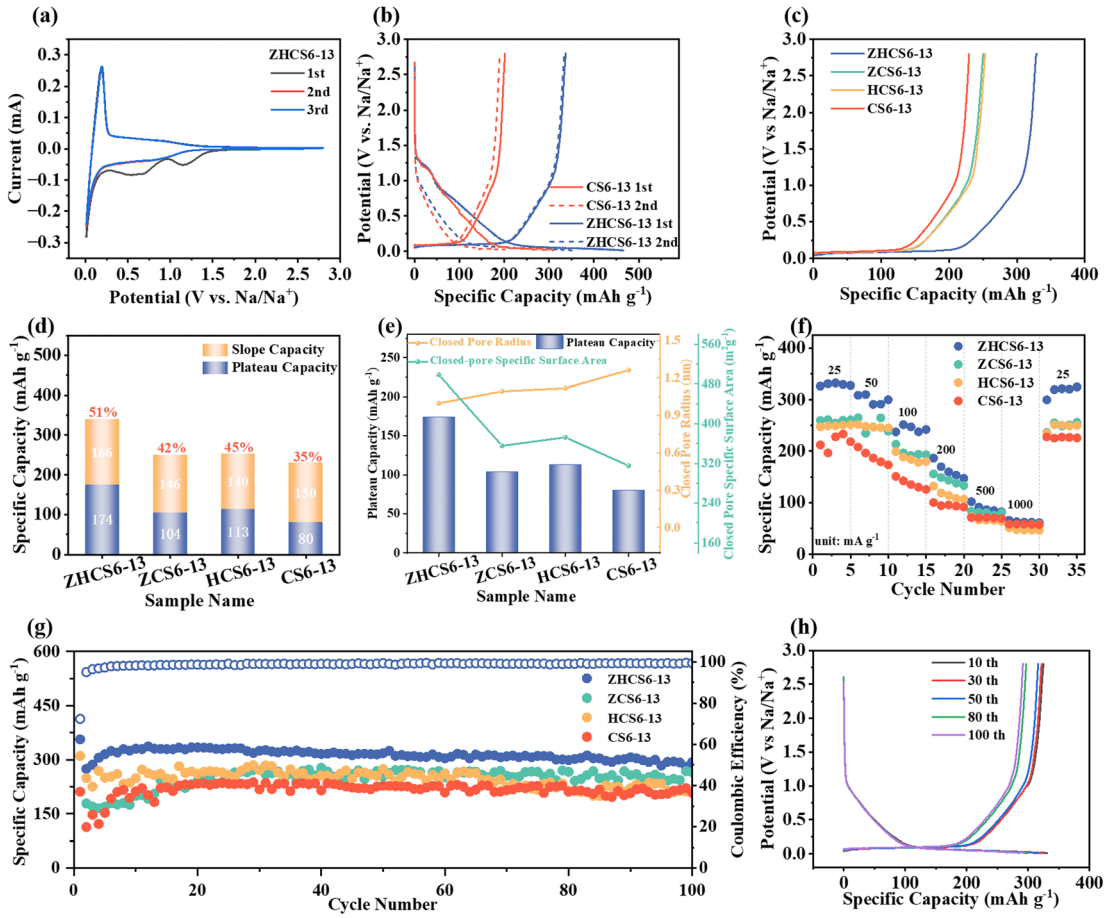

Fig. 4 (a) CV curves of ZHCS6-13 at 0.1 mV s^{-1}. (b) The GCD curves for the initial two cycles of ZHCS6-13 and CS6-13 at a current rate of 25 mA g^{-1}. (c) Charge curves comparison in the 25th cycle at 50 mA g^{-1}, and (d) the corresponding capacities in the plateau region and sloping region. (e) The relationships between plateau capacities and closed pore specific surface area/r_{SAXS}. (f) Rate capabilities from 25 to 1000 mA g^{-1}. (g) Cycling performance at 50 mA g^{-1}. (h) GCD curves of ZHCS6-13 at 50 mA g^{-1}.

To deeply investigate the electrochemical sodium storage performance of samples, we performed electrochemical measurements in half-cells. The CV curves with a voltage range of 0.01–2.8 V were first carried out (Fig. 4a and Fig. S8, ESI†). During the initial scan, all samples showed irreversible broad peaks, which is attributed to irreversible electrolyte decomposition and SEI film formation.[53] The CV curves almost overlapped in the next two cycles, suggesting that the SEI layer formation occurs primarily in the first cycle. In addition, all samples exhibit a sharp oxidation/reduction peak at around 0.1 V, corresponding to the reversible sodium filling in the closed pores.[40,54] In line with the CV curve, the GCD curve for all samples is also divided into two parts, including the low-voltage plateau region and the high-voltage sloping region (Fig. 4b and Fig. S9, ESI†), corresponding to sodium ions adsorbed on defective structures and sodium ions filled in closed pore structures, respectively. The initial two cycles of charge/discharge curves of the ZHCS6-13 anode exhibit a higher degree of overlap compared with the CS6-13 anode, indicating superior sodium ion storage reversibility. Additionally, ZHCS6-13 displayed an increase in initial discharge and charge specific capacity, reaching to 465 and 337 mA h g^{-1}, respectively, with a higher initial Coulombic efficiency (ICE) value of 73% compared with the CS6-13 anode (65%). According to previous reports,[24,55] solvated sodium ions can enter open pores, but not closed pores. The accessibility of pores to solvated sodium ions usually causes significant side reactions that reduce the ICE of hard carbons. As mentioned above, although the specific surface area of open pores of ZHCS6-13 is larger than CS6-13, since the solvated sodium ions present in the electrolyte are larger than the N_2, the surface area determined by gas adsorption doesn't necessarily represent the contact area between the liquid electrolyte and the electrode active materials.[56] In addition, the closed pore content of ZHCS6-13 is much higher than that of CS6-13, which results in a higher ICE for ZHCS6-13 due to the difference in pore distribution between the two. These results further suggest that ZHCS6-13 has less irreversible electrolyte decomposition and formed thinner and more stable SEI films during the initial GCD process.

As displayed in Fig. 4c and d, the increase in sodium storage ability is mainly proportion to the enhanced plateau capacities, from 80 mA h g^{-1} (35%) of CS6-13 to 174 mA h g^{-1} (51%) of ZHCS6-13. To further investigate the effect of closed pores structure on plateau capacity, we further explore the relationship between the specific surface area and the mean radius of closed pores and plateau capacity. As shown in Fig. 4e and Fig. S10 (ESI†), smaller r_{SAXS} and larger $S_{closed\ pores}$ are conducive to the filling of sodium ions in pores, and the plateau capacity of the samples has a amazing linear relationship with the specific surface area of the closed pores (R^2 = 0.996), which is conducive to improving the plateau capacities. Therefore, the synergistic effect of acid treatment and the ZnO template enable hard carbon to enables suitable closed pore radius and more closed pores for sodium ions storage, thus contributing to enhanced plateau capacity. Notably, ZHCS6-13 demonstrated exceptional specific capacity/plateau capacity that surpasses the majority of reported biomass derived hard carbon anodes (Table S3, ESI†).

Fig. 4f and Fig. S11 (ESI†) show the rate performance of samples. ZHCS6-13 exhibits the highest average capacity. In addition, when the current density is switched back to 25 mA g^{-1}, the capacity of the optimized carbon anodes can be restored to the initial level, demonstrating the robust structure of the closed pores and significant reversibility. Cycling stability tests were conducted at a current rate of 50 mA g^{-1} (Fig. 4g). As shown in Fig. 4h, the GCD curves of different cycles can coincide well, which indicates the excellent stability of sodium ions storage. This can be attributed to the fact that ZHCS6-13 has abundant and appropriately sized closed pores that provide more sodium ions storage sites in the low-voltage plateau region. The SEI has a significant impact on the ICE, cycling stability and charge transfer kinetics of the battery. Therefore, X-ray photoelectron spec-troscopy (XPS) analysis of ZHCS6-13 was conducted to analyze the composition of SEI after cycling. As shown in Fig. S12 (ESI†), the XPS results of the ZHCS6-13 electrode after cycling indicate that the SEI is composed of C, O and F. The Na–F groups in F 1s peaks may result from the decomposition of FEC.[57] The SEI of the ZHCS6-13 electrode contains a high concentration of inorganic components (sodium carbonate, sodium fluoride), particularly those containing F, which helps to improve the interface stability and efficient transport of sodium ions at the anode/electrolyte interphase.[45] These findings are consistent with the formation of stable SEI layers and excellent electrochemical properties.

CV measurements were carried out at various scan rates from 0.1 to 1 mV s^{-1} (Fig. 5a) to gain a deep insight into the reaction kinetics of the hard carbons. The relationship between scan rate (ν) and peak current (i) follows the **e**qn (1):[35]

$$i = a\nu^b \quad (1)$$

where i is the peak current, ν is the scan rate. Here, a value of b close to 0.5 signifies that the electrochemical reaction is primarily diffusion-controlled, while a value of b close to 1.0 suggests that capacitance-controlled behavior dominates. The b values of the oxidation peak (Peak 1) and reduction peak (Peak 2) in the CV curves for ZHCS6-13 were 0.45 and 0.37, respectively (Fig. 5b), indicating that the electrochemical behavior at the low-voltage plateau region is predominantly diffusion-controlled.[58] A b-value of less than 0.5 is a characteristic of hard carbon materials, as reported in studies.[31,45,47,50,53] This behavior may result from several factors, including the uneven insertion of sodium ions due to the irregular structure of hard carbon, the influence of the interface and electrolyte on the charge transfer process, and the fact that the electrode reaction is not solely controlled by diffusion. The quantitative contributions of capacitance-controlled and diffusion-controlled processes in CV curves at various scan rates can be determined by eqn (2).

$$i = k_1\nu + k_2\nu^{1/2} \quad (2)$$

where ν represents the scan rates, $k_1\nu$ and $k_2\nu^{1/2}$ correspond to the contributions of capacitance-controlled and diffusion-controlled

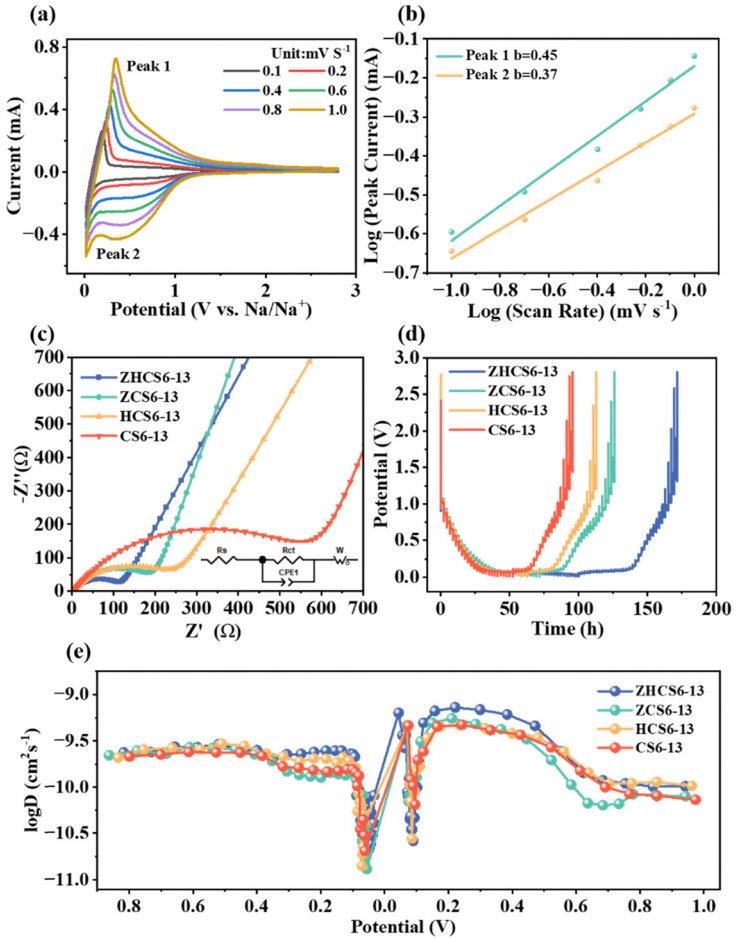

Fig. 5 (a) CV curves of ZHCS6-13 at various scanning rates from 0.1 to 1 mV s^{-1} and (b) the corresponding correlations between peak current (*i*) and scan rate (*v*) at peak 1 and peak 2. (c) Nyquist plots, and the inset is an equivalent electrical circuit model. (d) GITT curves of samples. (e) Sodium ions diffusion coefficients during the sodiation and desodiation process.

capacity, respectively. As displayed in Fig. S13 (ESI†), it is evident that the capacitive contribution tends to increase with rising scan rates. The capacitive contribution in the ZHCS6-13 increases from 45% at 0.1 mV s^{-1} to 72% at 1 mV s^{-1}, indicating the capacitive-controlled behavior with fast storage kinetics is dominant in the charge/discharge process at high current rates, and can also explain the significant loss of plateau capacity at high current densities.[53,59]

As displayed in Fig. 5c, the diffusion characteristics of the samples were analyzed by electrochemical impedance spectroscopy (EIS). The Nyquist plot consists of a semicircle at the high/middle-frequency regions and a line at the low- frequency region, corresponding to the charge-transfer resistance and ion diffusion resistance in the electrode, respectively. ZHCS6-13 has the smallest charge transfer resistance of 113 Ω (Table S2, ESI†), which indicates that microstructure regulation improves the electrical conductivity of the hard carbon. In addition, the calculation shows that the sloping line in the low-frequency region of ZHCS6-13 is the steepest and has the smallest impedance coefficient (Fig. S14, ESI†), showing fast transfer kinetics. This may be because the samples after the collaborative treatment have fewer defects and abundant closed pores with appropriate pore size, which collaborately enhance the electrochemical reaction kinetics of sodium ions during charge and discharge processes.

The sodium ions diffusion kinetics of the hard carbon anodes were studied by galvanostatic intermittent titration technique (GITT) measurements,[60] which is shown in Fig. 5d. The diffusion coefficient of sodium ions can be calculated by a simplified form of Fick's second law eqn (3).[24]

$$D_{Na^+} = \frac{4}{\pi\tau}\left(\frac{m_B V_m}{M_B S}\right)^2 \left(\frac{\Delta E_s}{\Delta E_t}\right)^2 \quad (3)$$

where τ represents the pulse duration, m_B and M_B refer to the active mass and molar mass of carbon, V_m is the molar volume, and S is the effective contact area. Additionally, ΔE_S is the potential change caused by the pulse, and ΔE_t is the potential change during constant current charging (discharging), which can be obtained from the GITT curve. As displayed in Fig. 5e, the D_{Na^+} values of all samples show a similar trend during the discharge and charging of the hard carbon anodes, which can be roughly divided into two parts.[31,32] The slope region (>0.1 V) is mainly attributed to the adsorption of sodium ions

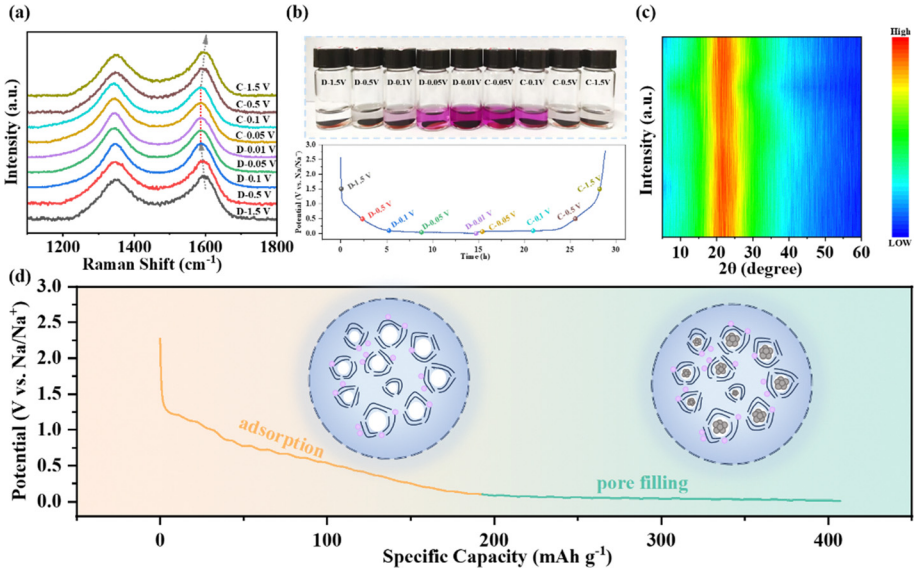

Fig. 6 (a) *Ex situ* Raman spectra (b) the corresponding color alteration of ethanol containing 1 wt% phenolphthalein after reaction with the ZHCS6-13 electrode at various potentials. (c) *Ex situ* XRD test of ZHCS6-13 electrode at selected potentials. (d) Schematic diagram of the sodium ions storage stages for ZHCS6-13.

at the defect active sites, which shows superior kinetic properties. The plateau region (<0.1 V) displays a sharp decline due to the filling of sodium ions in the closed pores surrounded by the carbon layers.[27,61] However, the plateau region remains controversial and needs to be combined with other tests to illustrate the sodium storage mechanism.

To study the mechanisms of sodium storage in the charge and discharge process, *ex situ* Raman, *ex situ* XRD and phenolphthalein tests were carried out. As displayed in Fig. 6a and Fig. S15a (ESI†), the G band shows a gradual red-shift from 1596 to 1586 cm^{-1} upon sodiation along the sloping region above 0.1 V, demonstrating that the electrons are transferred to the graphene sheets due to the adsorption of sodium ions.[62] In the plateau region below 0.1 V, the G band remains almost unchanged, indicating that electrons are no longer transferred to the graphene sheets.[53] Additionally, the color change of phenolphthalein ethanol solution was obvious during the whole charge–discharge process, as shown in Fig. 6b and Fig. S15b (ESI†). In particular, a clear red color appears in the voltage range of 0.1–0.01 V, which verifies the formation of quasi-metallic sodium inside the closed pores in the low-voltage plateau region.[62] Moreover, the formation and disappearance of the red color indicate the reversible evolution of the quasi-metallic sodium in the process of sodiation/desodiation. Furthermore, *ex situ* XRD shows that the position of the (002) peak has no obvious shift under different voltages (Fig. 6c), indicating that there is no significant sodium ion intercalation behavior in the pseudo-graphite structure in the whole charge–discharge process. Through comprehensive analysis of the above test results, the mechanism of sodium storage of the hard carbon is summarized in Fig. 6d. The slope capacity in the high-voltage region is attributed to the adsorption of sodium ions at the defect sites, while the plateau capacity in the low-voltage region is due to the closed pore filling of sodium clusters. Therefore, ZHCS6-13 with the largest number of closed pores has the best plateau capacity, which is conducive to the improvement of sodium storage performance.

As shown in Fig. 7a, to further evaluate the practical application prospect of the ZHCS6-13 anode, full sodium-ion cells were assembled by using the ZHCS6-13 anode and $Na_3V_2(PO_4)_3$ (NVP) cathode. The electrochemical performances of the NVP cathode in Na half-cells are displayed in Fig. S16 (ESI†). The GCD curves of ZHCS6-13//NVP at different current densities ranging from 25 to 500 mA g^{-1} are shown in Fig. 7b, clearly demonstrating stable charge/discharge voltage plateaus within the range of 3–3.5 V, indicating distinguished electrochemical stability. In addition, the full cells provide a high reversible capacity of 246 mA h g^{-1} (based on the mass of the anode material) at a current rate of 25 mA g^{-1}. As displayed in Fig. 7c, high capacity and cycling stability with a retention rate of 75% at a higher current of 500 mA g^{-1} after 100 cycles. Furthermore, the energy density (E, W h kg^{-1}) and power density (P, W kg^{-1}) of the sodium-ion full cells can be calculated by eqn (4) and (5).[32,53]

$$E = \int_{t_1}^{t_2} \frac{UI}{m} \mathrm{d}t \quad (4)$$

$$P = \frac{E}{t} \times 3600 \quad (5)$$

where I and U represent the discharge current (A) and operating voltage (V), respectively, m is the total mass (kg) of the anode and cathode, t (s) is time of the discharge. the energy density of the ZHCS6-13//NVP full cell was calculated to be 205.8 W h kg^{-1} at 21.9 W kg^{-1} and hold 95.4 W h kg^{-1} at 408.9 W kg^{-1}. These

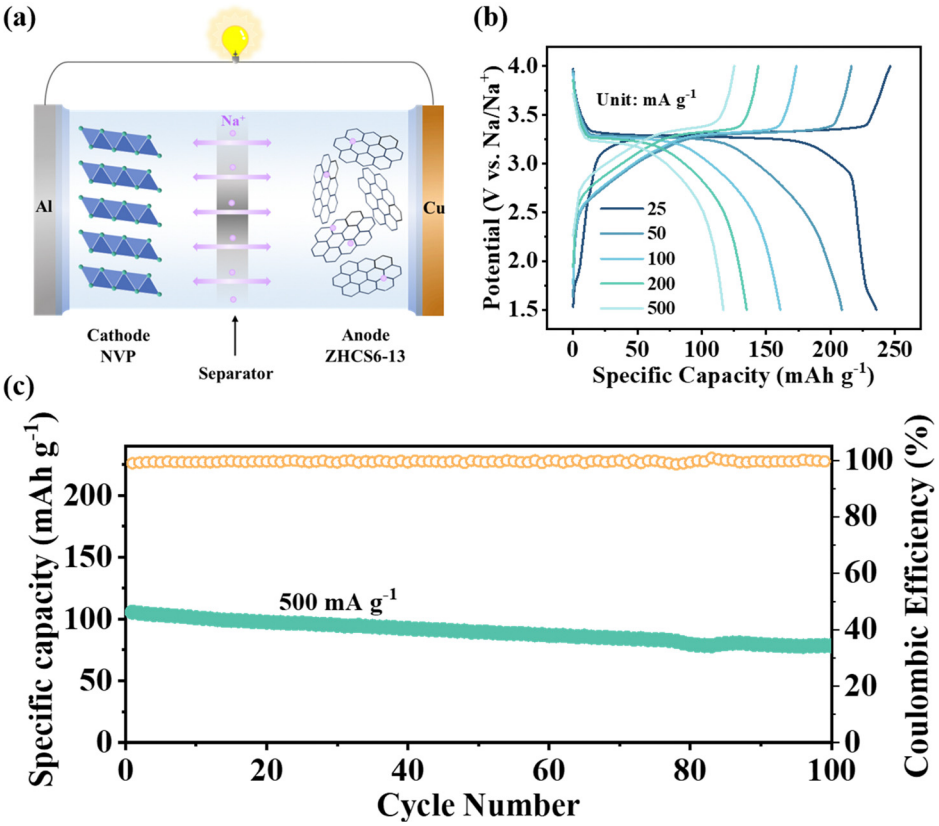

Fig. 7 Electrochemical properties of ZHCS6-13//NVP sodium-ion full cells. (a) Schematic illustration. (b) GCD curves at different current rates. (c) Cycling stability at 500 mA g^{-1} of ZHCS6-13//NVP sodium-ion full cells.

results suggest that ZHCS6-13 as an anode candidate shows a promising prospect in practical SIBs.

Conclusions

In summary, we combined the ZnO template method and acid treatment method to regulate the microstructure of hard carbon materials derived from camellia shells and successfully prepared hard carbon anode with high closed pore content. The acid treatment removed the resulting template ZnO and the inorganic ash from the biomass, leaving open pores, which form closed pores in the subsequent high-temperature treatment. The optimized ZHCS6-13 exhibits a considerable closed pore content and a suitable microstructure, with a reversible capacity of 340 mA h g^{-1} and a plateau capacity of 174 mA h g^{-1} at 50 mA g^{-1}. The storage performance of sodium ions is greatly improved. According to the *ex situ* Raman, *ex situ* XRD and phenolphthalein tests, the mechanism of sodium storage in the slope region and plateau region corresponds to the filling of defect sites and the formation of sodium clusters in closed pores, respectively. This work inspires precisely regulating the microporous structure of biomass-derived hard carbon materials to improve the performance of sodium ions storage and clarifies the intricate mechanism of hard carbon sodium storage derived from camellia shells, providing a theoretical basis for the design of high-performance hard carbon.

Author contributions

Ziying Zhang: methodology, conceptualization, investigation, formal analysis, writing – original draft. Yingxinjie Wang: resources, investigation, visualization. Zerui Chen: resources. Xiaohui Li: resources. Nan Zhang: resources. Zhenjun Wu: project administration, supervision, writing – review & editing. Xiuqiang Xie: project administration, supervision, writing – review & editing.

Data availability

The data supporting this article have been included as part of the ESI.†

Conflicts of interest

There are no conflicts to declare.

Acknowledgements

This research was financially supported by the National Natural Science Foundation of China (51977071, 52272295), the Natural Science Foundation of Hunan Province (2017JJ2040, 2020JJ4192) and the Science and Technology Innovation Program of Hunan Province (2021RC3066).

Notes and references

1 H. Li, Q. Ma, Y. Yuan, R. Wang, Z. Wang, Q. Zhang, L. Zhang, J. Zhu, S. Zhang, J. Mao, H. Li, S. Eliseeva, V. Kondratiev, Y. Zhang, C. Zhang and Y. Wu, *Adv. Funct. Mater.*, 2024, **34**, 2301987.
2 S. Zhou, Z. Tang, Z. Pan, Y. Huang, L. Zhao, X. Zhang, D. Sun, Y. Tang, A. S. Dhmees and H. Wang, *SusMat*, 2022, **2**, 357–367.
3 C. Liu, K. Chen, H. Xiong, A. Zhao, H. Zhang, Q. Li, X. Ai, H. Yang, Y. Fang and Y. Cao, *eScience*, 2024, **4**, 100186.
4 Q. Zhang, Z. Wang, S. Zhang, T. Zhou, J. Mao and Z. Guo, *Electrochem. Energy Rev.*, 2018, **1**, 625–658.
5 Y. Dong, Y. Chen, Q. Zeng, J. Feng, M. Fang, Z. Shi, J. Liu, Y. Sheng, X. Yue and Z. Liang, *Energy Mater. Adv.*, 2024, **5**, 0113.
6 E. Gabriel, C. Ma, K. Graff, A. Conrado, D. Hou and H. Xiong, *eScience*, 2023, **3**, 100139.
7 H. Tang, M. Wang, T. Lu and L. Pan, *Ceram. Int.*, 2017, **43**, 4475–4482.
8 A. Rudola, C. J. Wright and J. Barker, *Energy Mater. Adv.*, 2021, **2021**, 9798460.
9 R. H. Zhang, V. Raveendran, Y. N. He, A. Yau, A. Chang, C. Chi, S. Bong, F. Cheng, W. G. Ma and J. Chen, *Energy Mater. Adv.*, 2021, **2021**, 2124862.
10 Q. Li, D. Yang, H. Chen, X. Lv, Y. Jiang, Y. Feng, X. Rui and Y. Yu, *SusMat*, 2021, **1**, 359–392.
11 K. Nobuhara, H. Nakayama, M. Nose, S. Nakanishi and H. Iba, *J. Power Sources*, 2013, **243**, 585–587.
12 D. A. Stevens and J. R. Dahn, *J. Electrochem. Soc.*, 2001, **148**, A803.
13 N. Sun, J. Qiu and B. Xu, *Adv. Energy Mater.*, 2022, **12**, 2200715.
14 D. Chen, W. Zhang, K. Luo, Y. Song, Y. Zhong, Y. Liu, G. Wang, B. Zhong, Z. Wu and X. Guo, *Energy Environ. Sci.*, 2021, **14**, 2244–2262.
15 R. Dong, F. Wu, Y. Bai, Q. Li, X. Yu, Y. Li, Q. Ni and C. Wu, *Energy Mater. Adv.*, 2022, **2022**, 9896218.
16 X. Chen, N. Sawut, K. Chen, H. Li, J. Zhang, Z. Wang, M. Yang, G. Tang, X. Ai, H. Yang, Y. Fang and Y. Cao, *Energy Environ. Sci.*, 2023, **16**, 4041–4053.
17 N. Sun, Z. Guan, Y. Liu, Y. Cao, Q. Zhu, H. Liu, Z. Wang, P. Zhang and B. Xu, *Adv. Energy Mater.*, 2019, **9**, 1901351.
18 H. Chen, N. Sun, Y. Wang, R. A. Soomro and B. Xu, *Energy Storage Mater.*, 2023, **56**, 532–541.
19 T. W. Surta, E. Koh, Z. Li, D. B. Fast, X. Ji, P. A. Greaney and M. R. Dolgos, *Adv. Energy Mater.*, 2022, **12**, 2200647.
20 Y. Chu, J. Zhang, Y. Zhang, Q. Li, Y. Jia, X. Dong, J. Xiao, Y. Tao and Q. H. Yang, *Adv. Mater.*, 2023, **35**, 2212186.
21 X. Chen, J. Tian, P. Li, Y. Fang, Y. Fang, X. Liang, J. Feng, J. Dong, X. Ai, H. Yang and Y. Cao, *Adv. Energy Mater.*, 2022, **12**, 2200886.
22 C. Delmas, *Adv. Energy Mater.*, 2018, **8**, 1703137.
23 A. Kamiyama, K. Kubota, D. Igarashi, Y. Youn, Y. Tateyama, H. Ando, K. Gotoh and S. Komaba, *Angew. Chem., Int. Ed.*, 2021, **60**, 5114–5120.
24 K. Wang, F. Sun, H. Wang, D. Wu, Y. Chao, J. Gao and G. Zhao, *Adv. Funct. Mater.*, 2022, **32**, 2203725.
25 M. Yuan, B. Cao, H. Liu, C. Meng, J. Wu, S. Zhang, A. Li, X. Chen and H. Song, *Chem. Mater.*, 2022, **34**, 3489–3500.
26 Y. Li, Y. Lu, Q. Meng, A. C. S. Jensen, Q. Zhang, Q. Zhang, Y. Tong, Y. Qi, L. Gu, M. M. Titirici and Y. S. Hu, *Adv. Energy Mater.*, 2019, **9**, 1902852.
27 Q. Meng, Y. Lu, F. Ding, Q. Zhang, L. Chen and Y.-S. Hu, *ACS Energy Lett.*, 2019, **4**, 2608–2612.
28 W. Shao, Q. Cao, S. Liu, T. Zhang, Z. Song, C. Song, Z. Weng, X. Jian and F. Hu, *SusMat*, 2022, **2**, 319–334.
29 Y. Morikawa, S. i Nishimura, R. i Hashimoto, M. Ohnuma and A. Yamada, *Adv. Energy Mater.*, 2020, **10**, 1903176.
30 Y. Chen, Y. Wang, S. Zhu, K. Fu, X. Han, Y. Wang, B. Zhao, T. Li, B. Liu, Y. Li, J. Dai, H. Xie, T. Li, J. W. Connell, Y. Lin and L. Hu, *Mater. Today*, 2019, **24**, 26–32.
31 T. Xu, X. Qiu, X. Zhang and Y. Xia, *Chem. Eng. J.*, 2023, **452**, 139514.
32 X. Zhang, Y. Cao, G. Li, G. Liu, X. Dong, Y. Wang, X. Jiang, X. Zhang and Y. Xia, *Small*, 2024, **20**, 2311197.
33 P. Strubel, S. Thieme, T. Biemelt, A. Helmer, M. Oschatz, J. Brückner, H. Althues and S. Kaskel, *Adv. Funct. Mater.*, 2015, **25**, 287–297.
34 J. Yang, T. Feng, H. Zhou, C. Hu, Y. Guo, C. Chen, Z. Chen, J. Liu, G. Huang and M. Wu, *Cell Rep. Phys. Sci.*, 2020, **1**, 100186.
35 X. Yin, Z. Lu, J. Wang, X. Feng, S. Roy, X. Liu, Y. Yang, Y. Zhao and J. Zhang, *Adv. Mater.*, 2022, **34**, 2109282.
36 D. Igarashi, Y. Tanaka, K. Kubota, R. Tatara, H. Maejima, T. Hosaka and S. Komaba, *Adv. Energy Mater.*, 2023, **13**, 2302647.
37 N. Zhang, Q. Liu, W. Chen, M. Wan, X. Li, L. Wang, L. Xue and W. Zhang, *J. Power Sources*, 2018, **378**, 331–337.
38 X. Chen, C. Liu, Y. Fang, X. Ai, F. Zhong, H. Yang and Y. Cao, *Carbon Energy*, 2022, **4**, 1133–1150.
39 Z. Zheng, S. Hu, W. Yin, J. Peng, R. Wang, J. Jin, B. He, Y. Gong, H. Wang and H. J. Fan, *Adv. Energy Mater.*, 2024, **14**, 2303064.
40 L. Kitsu Iglesias, E. N. Antonio, T. D. Martinez, L. Zhang, Z. Zhuo, S. J. Weigand, J. Guo and M. F. Toney, *Adv. Energy Mater.*, 2023, **13**, 2302171.
41 L. Xiao, H. Lu, Y. Fang, M. L. Sushko, Y. Cao, X. Ai, H. Yang and J. Liu, *Adv. Energy Mater.*, 2018, **8**, 1703238.
42 Y. Li, Y. S. Hu, X. Qi, X. Rong, H. Li, X. Huang and L. Chen, *Energy Storage Mater.*, 2016, **5**, 191–197.
43 Z. Xu, J. Wang, Z. Guo, F. Xie, H. Liu, H. Yadegari, M. Tebyetekerwa, M. P. Ryan, Y. S. Hu and M. M. Titirici, *Adv. Energy Mater.*, 2022, **12**, 2200208.
44 A. Mahmood, Z. Yuan, X. Sui, M. A. Riaz, Z. Yu, C. Liu, J. Chen, C. Wang, S. Zhao, N. Mahmood, Z. Pei, L. Wei and Y. Chen, *Energy Storage Mater.*, 2021, **41**, 395–403.
45 Q. He, H. Chen, X. Chen, J. Zheng, L. Que, F. Yu, J. Zhao, Y. Xie, M. Huang, C. Lu, J. Meng and X. Zhang, *Adv. Funct. Mater.*, 2024, **34**, 2310226.
46 B. E. Warren, *Phys. Rev.*, 1941, **59**, 693–698.
47 D. Sun, L. Zhao, P. Sun, K. Zhao, Y. Sun, Q. Zhang, Z. Li, Z. Ma, F. Zheng, Y. Yang, C. Lu, C. Peng, C. Xu, Z. Xiao and X. Ma, *Adv. Funct. Mater.*, 2024, **34**, 2403642.

48 S. Feng, K. Li, P. Hu, C. Cai, J. Liu, X. Li, L. Zhou, L. Mai, B.-L. Su and Y. Liu, *ACS Nano*, 2023, **17**, 23152–23159.
49 W. Xu, H. Li, X. Zhang, T. Y. Chen, H. Yang, H. Min, X. Shen, H. Y. Chen and J. Wang, *Adv. Funct. Mater.*, 2024, **34**, 2309509.
50 L. Shang, R. Yuan, H. Liu, X. Li, B. Zhao, X. Liu, A. Li, X. Chen and H. Song, *Carbon*, 2024, **223**, 119038.
51 Z. Huang, X. Qiu, C. Wang, W. Jian, L. Zhong, J. Zhu, X. Zu and W. Zhang, *J. Energy Storage*, 2023, **72**, 108406.
52 D. Saurel, J. Segalini, M. Jauregui, A. Pendashteh, B. Daffos, P. Simon and M. Casas-Cabanas, *Energy Storage Mater.*, 2019, **21**, 162–173.
53 C. Qiu, A. Li, D. Qiu, Y. Wu, Z. Jiang, J. Zhang, J. Xiao, R. Yuan, Z. Jiang, X. Liu, X. Chen and H. Song, *ACS Nano*, 2024, **18**, 11941–11954.
54 P. Bai, Y. He, X. Zou, X. Zhao, P. Xiong and Y. Xu, *Adv. Energy Mater.*, 2018, **8**, 1703217.
55 Q. Li, Y. Zhu, P. Zhao, C. Yuan, M. Chen and C. Wang, *Carbon*, 2018, **129**, 85–94.
56 F. Wang, Z. Jiang, Y. Zhang, Y. Zhang, J. Li, H. Wang, Y. Jiang, G. Xing, H. Liu and Y. Tang, *eScience*, 2024, **4**, 100181.
57 M. Y. Sun, B. Liu, Y. Xia, Y. X. Wang, Y. Q. Zheng, L. Wang, L. Deng, L. Zhao and Z. B. Wang, *Adv. Mater.*, 2024, **36**, 2311432.
58 P. Lu, Y. Sun, H. Xiang, X. Liang and Y. Yu, *Adv. Energy Mater.*, 2018, **8**, 1702434.
59 Z. L. Xu, J. Park, G. Yoon, H. Kim and K. Kang, Small, *Methods*, 2019, **3**, 1800227.
60 H. Chen, N. Sun, Q. Zhu, R. A. Soomro and B. Xu, *Adv. Sci.*, 2022, **9**, 2200023.
61 Z. Zhu, W. Zhong, Y. Zhang, P. Dong, S. Sun, Y. Zhang and X. Li, *Carbon Energy*, 2021, **3**, 541–553.
62 S. Zhang, N. Sun, X. Li, R. A. Soomro and B. Xu, *Energy Storage Mater.*, 2024, **66**, 103183.

